Catalysis Today 160 (2011) 79–86

Contents lists available at ScienceDirect

Catalysis Today

journal homepage: www.elsevier.com/locate/cattod

Cs-modified iron nanoparticles encapsulated in microporous and mesoporous SiO_2 for CO_x-free H_2 production via ammonia decomposition

Yanxing Li[a,b], Lianghong Yao[a,b], Shunqiang Liu[b], Jing Zhao[b], Weijie Ji[b,*], Chak-Tong Au[a,**]

[a] Department of Chemistry, Center for Surface Analysis and Research, Hong Kong Baptist University, 224 Waterloo Road, Kowloon Tong, Hong Kong, China
[b] The Key Laboratory of Mesoscopic Chemistry, Ministry of Education, School of Chemistry and Chemical Engineering, Nanjing University, Nanjing 210093, China

ARTICLE INFO

Article history:
Available online 24 March 2010

Keywords:
Ammonia decomposition
Pure hydrogen
Encapsulation
Iron
Core–shell structure

ABSTRACT

The stable core–shell Fe@SiO_2 catalysts reported in this paper are highly efficient for the generation of CO_x-free H_2 through ammonia decomposition. By tuning the porosity of SiO_2 shells (using C_{18}TMS agent) and with the introduction of an appropriate amount of Cs dopant (via pre-deposition as well as post-impregnation), the diffusion efficiency of the catalysts and the surface property of Fe cores can be modified for better performance. The Fe@SiO_2 structures function as microcapsular-like reactors during ammonia decomposition. Naked nanoparticles of metallic iron tend to aggregate into bulk particles spontaneously. The role of the stable SiO_2 shells is to prevent the enwrapped core particles from aggregation at high reaction temperatures.

1. Introduction

In the last decade, core–shell structured materials have attracted wide attentions because of their unique structural feature and physicochemical properties [1–5]. Nanoparticles (NPs) coated with silica have been studied in the fields of biology, optics, electronics, magnetism, sensing, etc. [3,6]. By encapsulating the nanoparticles of materials in stable but porous shells, one can have the stability and compatibility of the core materials enhanced; in the mean time, the electron charge, reactivity and functionality of the enwrapped materials also changed [7,8]. As demonstrated by Grasset et al., the magnetic property of zinc ferrite would be changed when it was encapsulated by a silica shell [9]. Also, Sorensen et al. reported that the core–shell structured composites show specific properties that are different from those of the individual core or shell material [10].

The interaction of ammonia with metal surfaces has been extensively investigated [11–14]. The studies were undertaken primarily to acquire insights into the mechanism of ammonia synthesis. The catalytic decomposition of ammonia was also studied for the production of clean hydrogen used in fuel cells [10,15–18]. The production of hydrogen directly from carbonaceous substances (e.g., methanol, methane) has its limitation because the generated byproducts CO_x ($x = 1, 2$) degrade fuel cell performance even at extremely low concentrations [19–23]. Goodman and co-workers did pioneer works on catalytic ammonia decomposition, and provided valuable information for the understanding of catalyst systems and catalytic processes [15,20,21]. Compared with methanol reforming, ammonia decomposition is a more economical process for the production of pure hydrogen [24,25].

A wide range of materials have been studied for ammonia decomposition [26–28]. Ru was found to be the most active among the noble metals while Ni was the most attractive among the cheap metals [15,16]. Alkali, alkaline-earth, and several rare earth metals have showed promotion effect in catalytic ammonia decomposition. Han et al. reported the influence of iridium addition on nickel-based catalysts [29]. Raróg-Pilecka et al. found that with Cs modification the reaction rate over carbon-supported Ru can be greatly improved [30]. Yin et al. demonstrated that KOH modification of Ru/CNTs can remarkably decrease the apparent activation energy and thus increase activity [31]. A number of iron-based catalysts were also found to be effective for ammonia decomposition [32,33].

In this work, Cs-modified core–shell Fe@SiO_2 catalysts were synthesized for ammonia decomposition. In the case of Fe NPs encapsulated in the microporous SiO_2, Cs was introduced by pre-deposition as well as post-impregnation. In the case of Fe NPs encapsulated in the mesoporous SiO_2, the pore size of SiO_2 shell was tuned before Cs modification. In order to understand the physicochemical properties and the catalytic behaviors of the core–shell Fe@SiO_2 catalysts, the precursors and the catalysts were characterized by techniques such as N_2 adsorption–desorption measurement (BET), scanning electron microscopy (SEM), X-ray diffraction (XRD), transmission electron microscopy (TEM), H_2

* Corresponding author. Fax: +86 25 83317761.
** Corresponding author. Fax: +852 34117348.
E-mail addresses: jiwj@nju.edu.cn (W. Ji), pctau@hkbu.edu.hk (C.-T. Au).

0920-5861/$ – see front matter © 2010 Elsevier B.V. All rights reserved.
doi:10.1016/j.cattod.2010.02.066

temperature-programmed desorption (TPD) and X-ray photoelectron spectroscopy (XPS).

2. Materials and methods

2.1. Materials

Iron (III) nitrate nonahydrate ($Fe(NO_3)_3{\cdot}9H_2O$, >95%), urea (>99.0%), tetraethylorthosilicate (TEOS, 98%), octadecyltrimethoxysilane (C_{18}TMS, 90%) were all purchased from Sigma–Aldrich; Polyvinylpyrrolidone K-30 (PVP K-30, molecular weight in the range of 27,000–33,000) was obtained from Sinopharm Chemical Reagent Co., Ltd. Cesium nitrate ($CsNO_3$), concentrated ammonia aqueous solution ($NH_3{\cdot}H_2O$) and anhydrous ethanol (EtOH) were purchased from Nanjing Chemical Reagent Co., Ltd. All the chemicals were used as received.

2.2. Catalysts preparation

2.2.1. Fe_2O_3-NPs and Cs-modified Fe_2O_3-NPs

Fe_2O_3-NPs were prepared by a PVP-assisted hydrothermal method reported elsewhere [34]. Typically, 6.06 g of $Fe(NO_3)_3{\cdot}9H_2O$ was added to 40 ml of distilled water containing 0.9 g of PVP K-30 that had been stirred for 3 h at 313 K. After stirring for another 3 h, 9.0 g of urea was added. The obtained transparent orange solution was then transferred into a 50 ml Teflon-lined stainless steel autoclave and hydrothermally treated at 453 K for 24 h. The obtained precipitate was collected by centrifugation and washed three times with distilled water and ethanol. The sample that was dried at 373 K overnight and calcined in air at 823 K for 4 h is denoted as Fe_2O_3-NPs hereinafter.

To modify Fe_2O_3-NPs with Cs, 6.06 g of $Fe(NO_3)_3{\cdot}9H_2O$ and 0.147 g $CsNO_3$ (molar ratio of Cs/Fe = 0.05) were added to 40 ml of distilled water containing 0.9 g of PVP K-30, followed by stirring at 40 °C for 3 h. Then 9.0 g of urea was added. The steps that followed afterward were similar to those adopted for the preparation of Fe_2O_3-NPs. The obtained sample is denoted as Cs-Fe_2O_3-NPs hereinafter.

2.2.2. Microporous silica-encapsulated Fe_2O_3-NPs and the Cs-modified catalysts

Fe_2O_3@SiO_2 core–shell structures were prepared by a sonication-assisted Stöber process [35]. Typically, 1.0 g of Fe_2O_3-NPs or 1.0 g of Cs-Fe_2O_3-NPs was added to 100 ml anhydrous ethanol and sonicated for 30 min in an ultrasound bath (KQ-100DE, 40 kHz, 100 W). Then 10 ml of $NH_3{\cdot}H_2O$ and a designated amount of tetraethylorthosilicate (TEOS) were added under sonication. After 1 h, the products were collected by centrifugation, washed two times with distilled water and ethanol, and dried at 353 K for 6 h. The obtained sample is denoted hereinafter Fe_2O_3@micro-SiO_2 or Cs-Fe_2O_3@micro-SiO_2, respectively.

In the case of post-impregnation, 1.0 g of Fe_2O_3@micro-SiO_2 was added to 50 ml ethanol containing 0.122 g of $CsNO_3$. The Cs/Fe molar ratio was 0.05. The mixture was stirred at 333 K for 6 h and dried in a rotary evaporator at 323 K. The sample was then subjected to calcination at 823 K for 2 h. The as-obtained catalyst is denoted hereinafter as Fe_2O_3@micro-SiO_2-Cs.

2.2.3. Mesoporous silica-encapsulated Fe_2O_3-NPs and the Cs-modified catalysts

First, 1.0 g of Fe_2O_3-NPs was added to a solution containing 100 ml of anhydrous ethanol and 10 ml of deionized water and the resulting mixture was sonicated for 30 min. After that 10 ml of iso-PrOH solution containing a certain amount of tetraethylorthosilicate (the molar ratio of Fe/Si = 5/1) and C_{18}TMS was added dropwise, and 10 ml of $NH_3{\cdot}H_2O$ was then injected. After reaction at 313 K for 6 h, the products were collected by centrifugation, washed with distilled water and ethanol twice and dried at 353 K for 6 h. Finally, the sample was calcined at 823 K for 2.5 h. The samples prepared with C_{18}TMS/TEOS molar ratio being 0.33, 0.2, and 0.05 are denoted as Fe_2O_3@meso-SiO_2 (0.33), Fe_2O_3@meso-SiO_2 (0.2), and Fe_2O_3@meso-SiO_2 (0.05), respectively.

The impregnation of Fe_2O_3@meso-SiO_2 with an ethanol solution of $CsNO_3$ was also applied and the procedure was the same as that adopted for the preparation of Fe_2O_3@micro-SiO_2-Cs. The Cs/Fe atomic ratio was 0.05. The corresponding samples are denoted as Fe_2O_3@meso-SiO_2-Cs (0.03), Fe_2O_3@meso-SiO_2-Cs (0.2), and Fe_2O_3@meso-SiO_2-Cs (0.05), respectively.

The oxidic core–shell catalysts were subjected to *in situ* reduction in a H_2–Ar mixture (H_2/Ar volume ratio = 1/3) at 823 K for 2 h before activity measurement. In all cases, once Fe_2O_3 cores are transformed into metallic Fe, the denotation of samples would be accordingly altered.

2.3. Catalytic testing

Catalytic testing was carried out in a continuous-flow quartz reactor (catalyst: 0.1 g, 60–80 mesh) under pure NH_3 (flow rate = 50 ml/min, $GHSV_{NH3}$ = 30,000 ml/(h g_{cat})). Before testing, the catalyst was *in situ* reduced in a 25% H_2/Ar flow at 823 K for 2 h. With the introduction of pure NH_3, activity results in the 673–973 K range were recorded once the reaction was stabilized at a particular temperature. Product analysis was performed on an on-line gas chromatograph (GC-122) equipped with thermal conductive detector and Poropak Q column, using He as carrier gas. NH_3 conversion in a blank reactor was <1.0% at 823 K.

2.4. Catalyst characterization

BET surface area and pore size distribution were measured on a NOVA-1200 Material Physical Structure Determinator. Prior to measurement, the catalyst was degassed at 573 K for 2 h. XRD analysis was performed on a Philips X'Pert MPD Pro X-ray diffractometer with graphite monochromatized Cu Kα radiation (λ = 0.1541 nm). SEM measurements were carried out on a LEO 1450VP scanning microscope. (HR)TEM images were taken on a JEOL JEM-2100 electron microscope operated at 200 kV. H_2-TPD experiments were carried out to estimate the exposure of surface metal. Before each measurement, the sample (0.3 g) was heated to 873 K in a flow of 25% H_2/Ar at a rate of 10 K/min, and kept at this temperature for 1 h. After cooling to room temperature (RT) and kept at RT for 0.5 h, the sample was purged with He gas at 323 K for 0.5 h. Then the catalyst was heated at a rate of 10 K/min while the H_2-TPD curve was recorded. XPS measurement was performed on a Leybold Heraeus-Shengyang SKL-12 electron spectrometer equipped with a VG CLAM 4 MCD electron energy analyzer, using Al Kα as excitation source.

3. Results and discussion

3.1. Physical properties

Table 1 depicts the physical characteristics of the core–shell catalysts. In general, with the addition of Cs, there is remarkable decrease in specific surface area. For example, with Cs impregnation, the surface area of Fe@micro-SiO_2 declines from 37 to 16 m^2/g. The specific surface areas of Fe@meso-SiO_2 (0.33), Fe@meso-SiO_2 (0.2), and Fe@meso-SiO_2 (0.05) were 165, 154, and 101 m^2/g, respectively. The large surface areas of the catalysts are originated from the mesopores of the shells, and are affected by the amount of C_{18}TMS used during preparation. The results confirm

Table 1
Physical properties of catalysts.

Catalyst	S_{BET} (m^2/g)	Pore volume (cm^3/g)	Pore diameter (nm)
Fe@micro-SiO_2 (Ref. [34])	35	–	44
Cs-Fe@micro-SiO_2	37	–	47
Fe@micro-SiO_2-Cs	16	–	50
Fe@meso-SiO_2 (0.33)	165	0.208	4.1
Fe@meso-SiO_2 (0.2)	154	0.186	4.4
Fe@meso-SiO_2 (0.05)	101	0.153	6.2
Fe@meso-SiO_2-Cs (0.33)	51	–	50
Fe@meso-SiO_2-Cs (0.2)	45	–	55
Fe@meso-SiO_2-Cs (0.05)	41	–	60

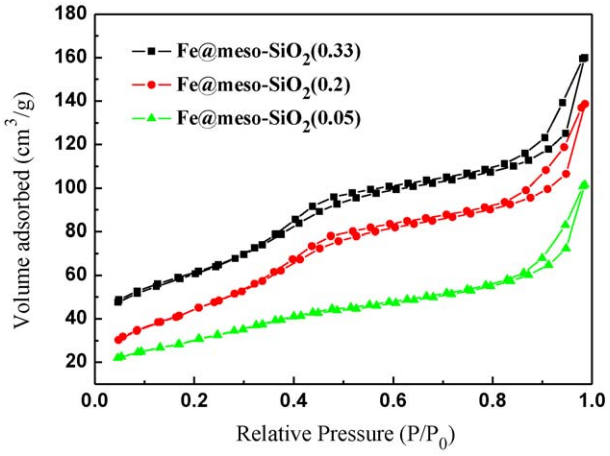

Fig. 1. Nitrogen adsorption and desorption isotherms of Fe@meso-SiO_2 (0.33), Fe@meso-SiO_2 (0.2), and Fe@meso-SiO_2 (0.05).

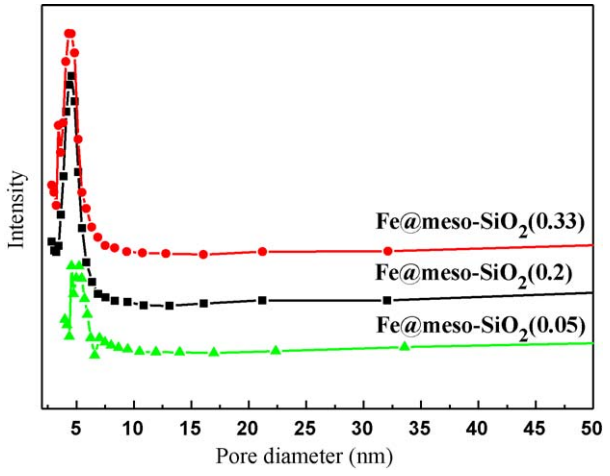

Fig. 2. Pore distribution of Fe@meso-SiO_2 (0.33), Fe@meso-SiO_2 (0.2), and Fe@meso-SiO_2 (0.05).

that the porosity of SiO_2 shell can be effectively tuned by altering the amount of C_{18}TMS. Figs. 1 and 2 show, respectively, the N_2 adsorption–desorption isotherms and pore size distributions of Fe@meso-SiO_2 (0.33), Fe@meso-SiO_2 (0.2), and Fe@meso-SiO_2 (0.05). All the samples show hysteresis loop of type-IV isotherms with the sudden increase at P/P_0 = 0.3–0.4 and display pore size distribution of 4–10 nm, suggesting that the mesopores created by employing C_{18}TMS are well ordered. With the inclusion of Cs, the corresponding surface area dropped to 51, 45, and 41 m^2/g while there are sharp increases in pore diameter (from 4.1, 4.4, and 6.2 nm to 50, 55, and 60 nm, respectively). The wide pores may be arisen from the stacking of the core–shell NPs.

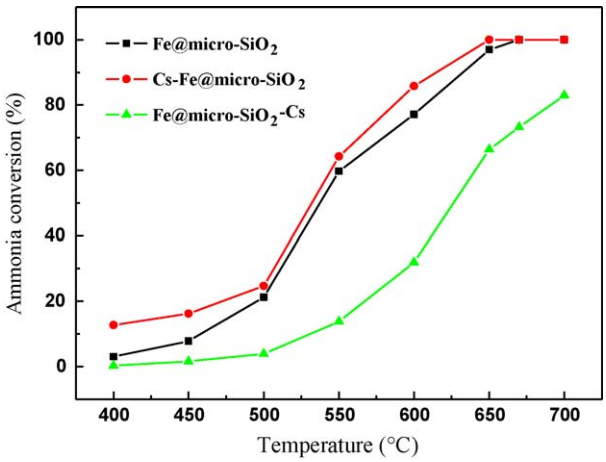

Fig. 3. Temperature dependence of ammonia conversion over Fe@micro-SiO_2, Cs-Fe@micro-SiO_2 and Fe@micro-SiO_2-Cs.

3.2. Catalytic activity

Figs. 3 and 4 show the temperature dependence of ammonia conversion over the catalysts while Table 2 depicts the hydrogen formation rates. From Fig. 3 one can see that Fe@micro-SiO_2-Cs (Cs was introduced by post-impregnation) is inferior to the other three catalysts with microporous shells. Nonetheless, Cs-Fe@micro-SiO_2 performs better than Fe@micro-SiO_2. The results suggest that the effectiveness of Cs modification is strongly dependent on the way through which Cs is introduced. The Cs species can cause serious plugging of micropores, leading to decline of diffusion efficiency and reduced exposure of core metal. In order to avoid this problem, the mesoporous SiO_2 shells were generated by employing C_{18}TMS and the size of mesopores was somewhat modified by varying the TEOS/C_{18}TMS ratio (Table 1). Overall, the Cs-doped catalysts perform better than the un-doped counterparts (Fig. 4). The creation of mesopores ensures easy migration of Cs onto the enwrapped Fe NPs, and the promotion effect of Cs is apparent. Over the Fe@meso-SiO_2 (0.33)-Cs, Fe@meso-SiO_2 (0.2)-Cs, and Fe@meso-SiO_2 (0.05)-Cs catalysts, 100% ammonia conversion can be achieved at temperatures as low as 650 °C.

In ammonia synthesis, alkali and alkaline-earth elements have been used to promote supported Ru or Fe catalysts [36,37]. They are also known to be effective in preventing Ru and Fe particles from sintering. Forni et al. [38] compared the promoting effect of Cs, Ba, and K and concluded that they show an order of Cs > Ba > K. In the present study, we adopted the Cs element to modify the core–shell structured Fe@SiO_2. The Cs dopant can enhance the electron property of core surface, a favorable factor for reactant adsorption and reaction. Such an effect is strongly dependent on how Cs is introduced into the system. In other words, the Cs promoting effect is dependent on where the Cs dopant is located.

3.3. Morphology of the core–shell structures

Fig. 5 shows the SEM images of Fe@meso-SiO_2 as well as naked Fe_2O_3-NPs. The size of the core–shell structures is in the 60–100 nm range, and particle dispersion and shell roughness appear to be different across the samples. One can see that Fe@meso-SiO_2 (0.2) shows the highest particle dispersion while Fe@meso-SiO_2 (0.05) the highest shell roughness. The higher roughness of shell is due to the higher porosity of shell, in agreement with the results of N_2 adsorption–desorption measurement (Table 1). Therefore, by changing the Si/Fe and TEOS/C_{18}TMS ratios during catalyst preparation, one can modify the characteristics of the core–shell catalysts.

Table 2
H_2 formation rates (mmol/g_{cat} min) over catalysts.

Temp. (K)	673	723	773	823	873	923	943	973
Catalyst								
Fe-NPs (Ref. [34])	0.10	0.94	2.85	11.82	20.76	22.80	23.77	25.88
Fe@micro-SiO_2(Ref. [34])	1.00	2.61	7.13	19.99	25.81	32.48	33.48	33.48
Cs-Fe@micro-SiO_2	4.25	5.42	8.27	21.52	28.73	33.48	33.48	33.48
Fe@micro-SiO_2-Cs	0.07	0.54	1.31	4.62	10.69	22.23	24.51	27.79
Fe@meso-SiO_2 (0.33)	1.37	2.85	5.86	16.27	25.78	31.41	33.48	33.48
Fe@meso-SiO_2 (0.2)	1.31	2.81	8.67	20.46	26.18	31.57	33.48	33.48
Fe@meso-SiO_2 (0.05)	0.97	2.31	7.60	18.68	25.68	30.84	33.48	33.48
Fe@meso-SiO_2-Cs (0.33)	2.68	5.19	8.87	19.42	28.06	33.48	33.48	33.48
Fe@meso-SiO_2-Cs (0.2)	2.21	4.25	11.32	22.90	30.30	33.48	33.48	33.48
Fe@meso-SiO_2-Cs (0.05)	1.77	3.82	9.11	20.62	29.40	33.48	33.48	33.48

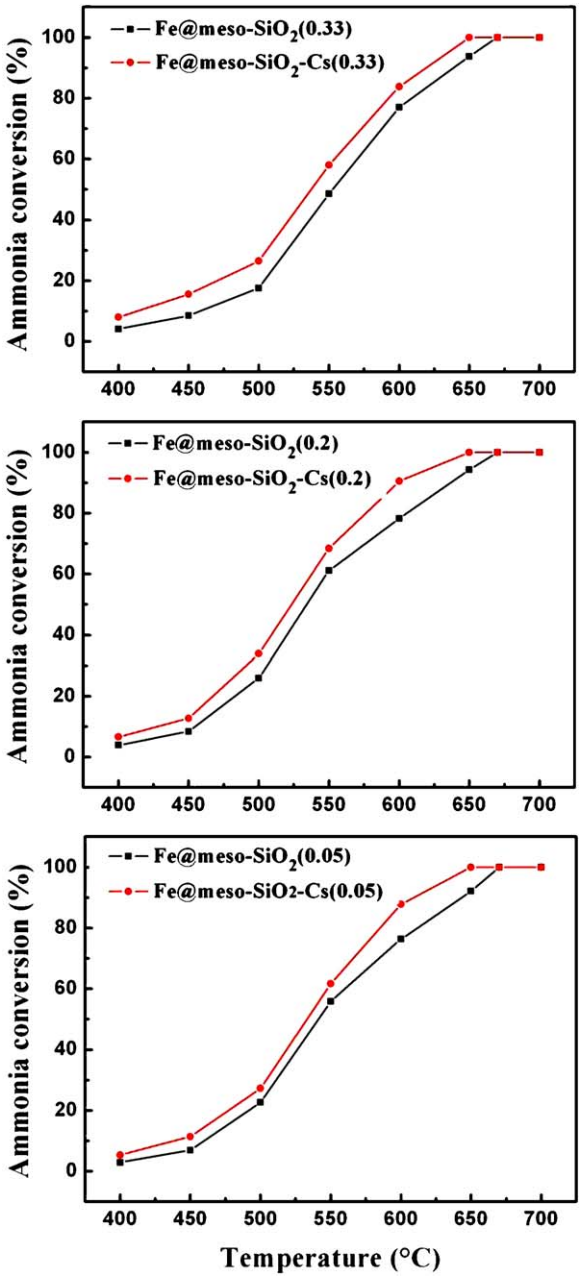

Fig. 4. Temperature dependence of ammonia conversion over Fe@meso-SiO_2 (0.33), Fe@meso-SiO_2-Cs (0.33), Fe@meso-SiO_2 (0.2), Fe@meso-SiO_2-Cs (0.2), Fe@meso-SiO_2 (0.05), and Fe@meso-SiO_2-Cs (0.05).

Shown in Fig. 6 are the TEM images of Fe_2O_3@micro-SiO_2, Fe@micro-SiO_2, Fe_2O_3@meso-SiO_2, and Fe@meso-SiO_2. In the cases of Fe_2O_3@micro-SiO_2 and Fe@micro-SiO_2, there are encapsulated Fe_2O_3 and Fe NPs showing core diameter of ca. 50 nm and shell thickness of <10 nm. For the Fe_2O_3@meso-SiO_2 and Fe@meso-SiO_2 samples, the Fe_2O_3 and Fe cores are a bit larger (60–100 nm). Note that the shells of Fe_2O_3@micro-SiO_2 and Fe@micro-SiO_2 are smoother and denser than those of Fe_2O_3@meso-SiO_2 and Fe@meso-SiO_2. The observations are in accordance with the results of SEM and N_2 adsorption–desorption measurements. From the TEM images, one can observe the decrease of core size after H_2-reduction, ascribable to the transformation of Fe_2O_3 to metallic Fe. From the insets of Fig. 6c and d, one can conclude that the Fe_2O_3 cores are polycrystalline while the Fe cores are highly crystallized.

3.4. Metal dispertion

Fig. 7 shows the XRD patterns of the core–shell structures before H_2-reduction. All the samples show the patterns of α-Fe_2O_3 phase (JCPDS No. 01-1053). No peaks of SiO_2 can be identified, suggesting the SiO_2 shells are essentially amorphous. There is a small peak assignable to Cs_2O phase ($2\theta = 28.4^\circ$, JCPDS No. 09-0104) observed over Fe_2O_3@micro-SiO_2-Cs and Fe_2O_3@meso-SiO_2-Cs (0.2) but not over Cs-Fe_2O_3@micro-SiO_2. The XRD results suggest that the dispersion of Cs is dependent upon the way of its introduction. It is obvious that in the cases of post-impregnation, due to the plugging of micropores Cs accumulates on the external wall of SiO_2 shells and becomes poor in dispersion.

Shown in Fig. 8 are the XRD patterns of Fe@micro-SiO_2, Fe@micro-SiO_2-Cs and Fe@meso-SiO_2-Cs (0.2). The samples show peaks of metallic Fe (JCPDS No. 01-1262), suggesting that the complete reduction of Fe_2O_3. We do not detect any signal of Cs over Fe@micro-SiO_2-Cs, indicating that the H_2-reduction treatment enhances the dispersion of Cs.

Fig. 9 illustrates the H_2-TPD profiles of Fe-NPs, Fe@micro-SiO_2, Fe@meso-SiO_2 (0.2), and Fe@meso-SiO_2-Cs (0.2). The onset desorp-

Table 3
H_2 uptake, surface Fe exposure and activation energy (E_a) over catalysts.

Sample	H_2-TPD		E_a (kJ/mol)
	H_2 uptake (μmol/g)	Surface Fe atoms per gram of catalyst	
Fe-NPs	3.76	2.26×10^{18}	105.1
Fe@micro-SiO_2	4.24	2.55×10^{18}	73.0
Cs-Fe@micro-SiO_2	4.75	2.86×10^{18}	60.8
Fe@micro-SiO_2-Cs	3.48	2.09×10^{18}	112.3
Fe@meso-SiO_2 (0.33)	5.08	3.06×10^{18}	69.3
Fe@meso-SiO_2 (0.2)	5.22	3.14×10^{18}	66.9
Fe@meso-SiO_2 (0.05)	5.28	3.18×10^{18}	68.2
Fe@meso-SiO_2-Cs (0.33)	7.10	4.27×10^{18}	62.8
Fe@meso-SiO_2-Cs (0.2)	7.36	4.43×10^{18}	60.1
Fe@meso-SiO_2-Cs (0.05)	8.03	4.83×10^{18}	62.5

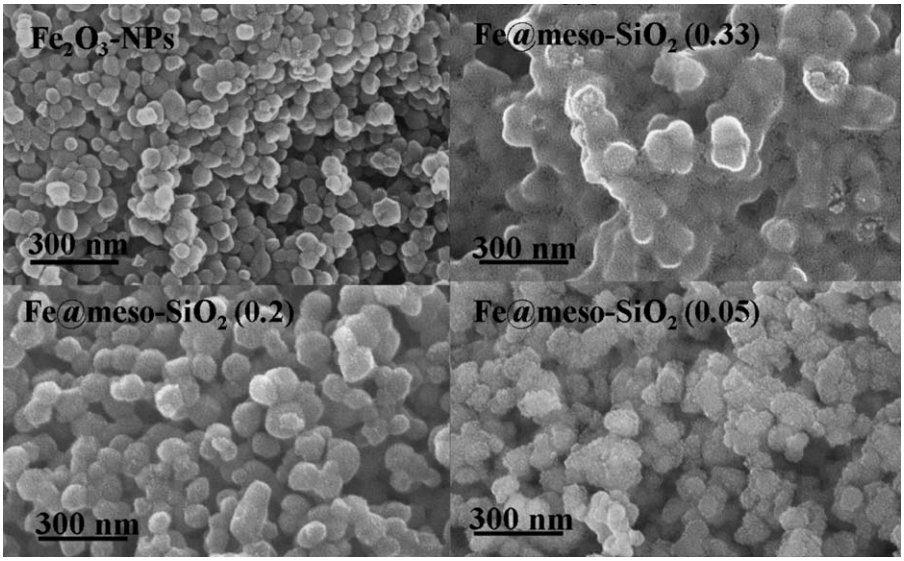

Fig. 5. SEM images of Fe_2O_3-NPs, Fe@meso-SiO_2 (0.33), Fe@meso-SiO_2 (0.2), and Fe@meso-SiO_2 (0.05).

tion temperatures are almost the same, ca. 80 °C. However, both the peak profile and temperature are different across the four catalysts: Fe@meso-SiO_2 (0.2) is the lowest in peak temperature (ca. 150 °C), about 25 °C lower than that of Fe@micro-SiO_2.

The Cs-doped catalyst shows the largest desorption peak, an indication of enhanced H_2 adsorption due to Cs doping. Based on peak areas and assuming an adsorption of one H atom per metal atom, the H_2 uptake can be estimated on the basis of a standard calibration procedure of CuO reduction. As depicted in Table 3, the encapsulated catalysts show higher H_2 uptake than Fe-NPs, with Fe@micro-SiO_2-Cs being the only exception. Among the Cs-free catalysts, Fe@meso-SiO_2 (0.05) shows the largest H_2 uptake (5.28 μmol/g) whereas among the Cs-doped catalysts, Fe@meso-SiO_2-Cs (0.05) shows the largest H_2 uptake (8.03 μmol/g). Obviously, the encapsulation of Fe nanoparticles with Cs modification results in enhanced H_2 adsorption capacity. It is understood that a larger uptake of hydrogen implies bigger exposure of surface Fe atoms and/or easy adsorption process. One can see that Fe@meso-SiO_2 (0.05) shows larger H_2 uptake than Fe@micro-SiO_2, and the result suggests that the shell porosity has an effect on the amount of exposed surface Fe atoms. A more obvious trend can be seen over Fe@meso-SiO_2-Cs (0.05) and Fe@micro-SiO_2-Cs, and this is because the porosity of shells can notably influence the location of Cs: in the latter case, the blocking of micropores by Cs is relatively more serious, causing a decline in effectiveness of surface atoms of Fe cores. On the other hand, the way of introducing Cs has an impact on surface exposure of cores: Fe@micro-SiO_2-Cs prepared by post-impregnation shows lower exposure of core metal than Cs-Fe@micro-SiO_2 prepared via pre-deposition. Note that based on TEM results, the surface exposure of core metal detected in the present study is lower than that of Ni/SiO_2 [15] and K-doped Ni/MCM-41 [39]. Our previous study [39] revealed that H_2 adsorption on silica material is negligible. Therefore, the H_2 spillover effect, viz. the migra-

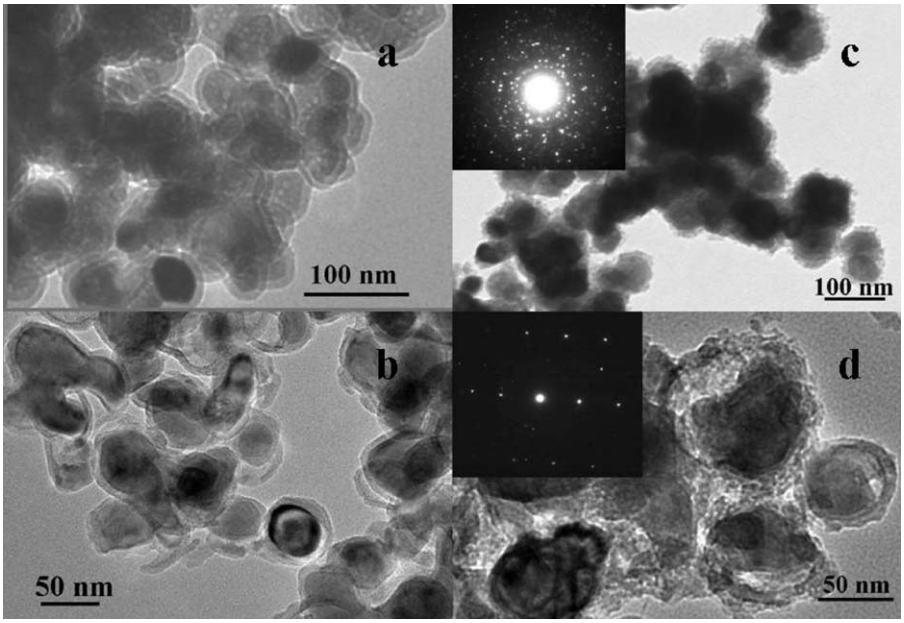

Fig. 6. TEM images of (a) Fe_2O_3@micro-SiO_2; (b) Fe@micro-SiO_2; (c) Fe_2O_3@meso-SiO_2 (0.2); (d) Fe@meso-SiO_2 (0.2).

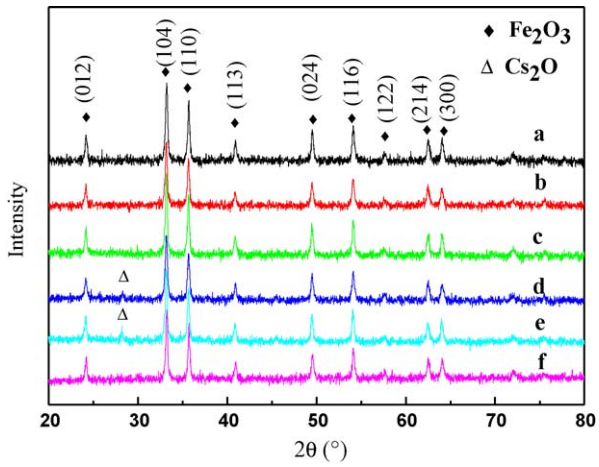

Fig. 7. XRD patterns of the catalysts before reduction: (a) Fe_2O_3-NPs; (b) Fe_2O_3@micro-SiO_2; (c) Fe_2O_3@meso-SiO_2 (0.2); (d) Fe_2O_3@micro-SiO_2-Cs; (e) Fe_2O_3@meso-SiO_2-Cs (0.2); (f) Cs-Fe_2O_3@micro-SiO_2.

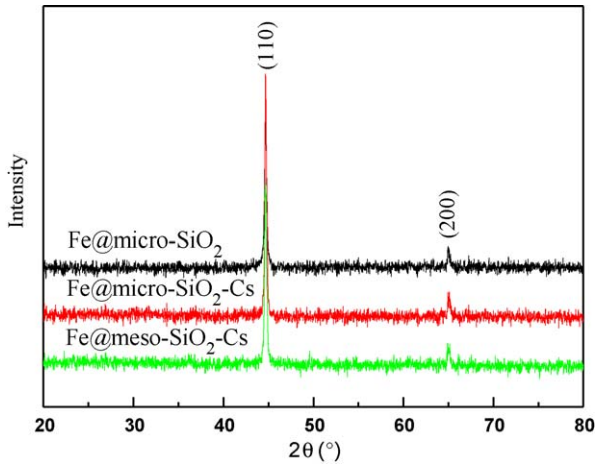

Fig. 8. XRD patterns of Fe@micro-SiO_2, Fe@micro-SiO_2-Cs, and Fe@meso-SiO_2-Cs (0.2) after H_2-reduction.

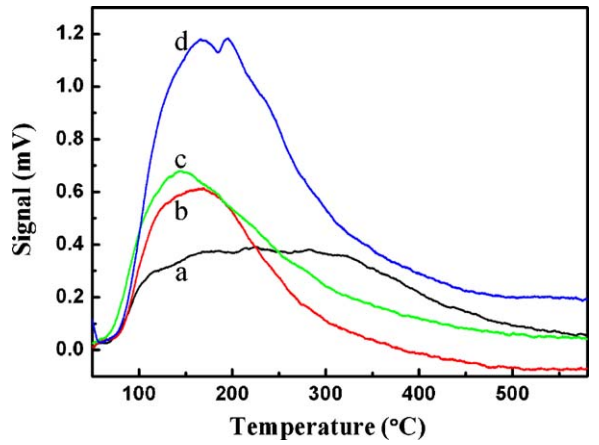

Fig. 9. H_2-TPD profiles of (a) Fe NPs, (b) Fe@micro-SiO_2, (c) Fe@meso-SiO_2 (0.2), and (d) Fe@meso-SiO_2-Cs (0.2).

tion of surface H onto silica surface should be insignificant. It is hence considered that the employment of the H_2-TPD method is a suitable for the determination of H_2 uptake in this catalyst system.

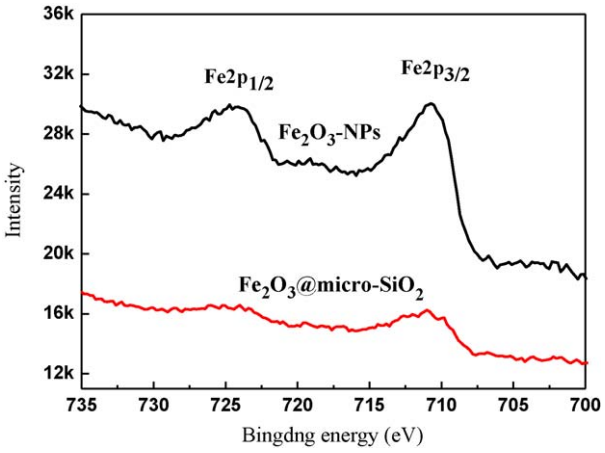

Fig. 10. Fe 2p spectra of Fe_2O_3-NPs and Fe_2O_3@micro-SiO_2.

3.5. Core–shell interaction

XPS technique was used to characterize the as-synthesized catalysts. Fig. 10 shows the Fe 2p spectra of Fe_2O_3-NPs and Fe_2O_3@micro-SiO_2. The Fe 2p signal of the latter is much weaker than that of the former, a result of the encapsulation of Fe_2O_3 by thin SiO_2 shells [40,41]. The Fe $2p_{1/2}$, Fe $2p_{3/2}$, and O 1s binding energies (BEs) of Fe_2O_3@micro-SiO_2 are slightly higher than those of naked NPs (Table 4), plausibly due to core–shell interaction. The Fe $2p_{1/2}$ and Fe $2p_{3/2}$ BEs reveal that the oxidation state of Fe is 3+, in consistent with the XRD results.

3.6. Activation energy

The turnover frequency (TOF) of the reaction over the catalysts within the temperature range of 823 ± 50 K was calculated by normalizing the observed H_2 formation rate (mmol/min g_{cat}) to the number of exposed Fe per gram of catalyst. From the Arrhenius plots shown in Fig. 11 one can obtain the apparent activation energies (E_a) which are depicted in Table 3. All the core–shell catalysts (ranging from 60 to 73 kJ/mol) with Fe@micro-SiO_2-Cs being the only exception (112.3 kJ/mol) show the E_a values lower than that of Fe-NPs (105.1 kJ mol^{-1}). The results are in agreement with the performance of the catalysts (Figs. 3 and 4). It is reasonable because a catalyst with lower E_a is inherently more active than the one with higher E_a. Note that the superior activity of the core–shell catalysts is not only from the contribution of the cores but also vitally from the exclusive core–shell environment in which the adsorption and reaction on the cores are obviously enhanced.

It is worth noting that the effect of SiO_2 presence on mass transfer should be minor due to the fact that the SiO_2 shell is not only porous but also very thin (ca. 10 nm). Furthermore, the reactant can be enriched in the space between the core and the internal wall of the shell, thus an enhanced adsorption and reaction occurs on the core surface. In other words, the surface reaction is not diffusion limited, and the kinetic data obtained is primary and reliable.

Table 4
Fe 2p and O 1s binding energies of Fe_2O_3-NPs and Fe_2O_3@micro-SiO_2.

	Binding energy (eV)		
	Fe $2p_{1/2}$	Fe $2p_{3/2}$	O 1s
Fe_2O_3-NPs	724.1	710.5	529.7
Fe_2O_3@micro-SiO_2	724.5	710.7	533.1

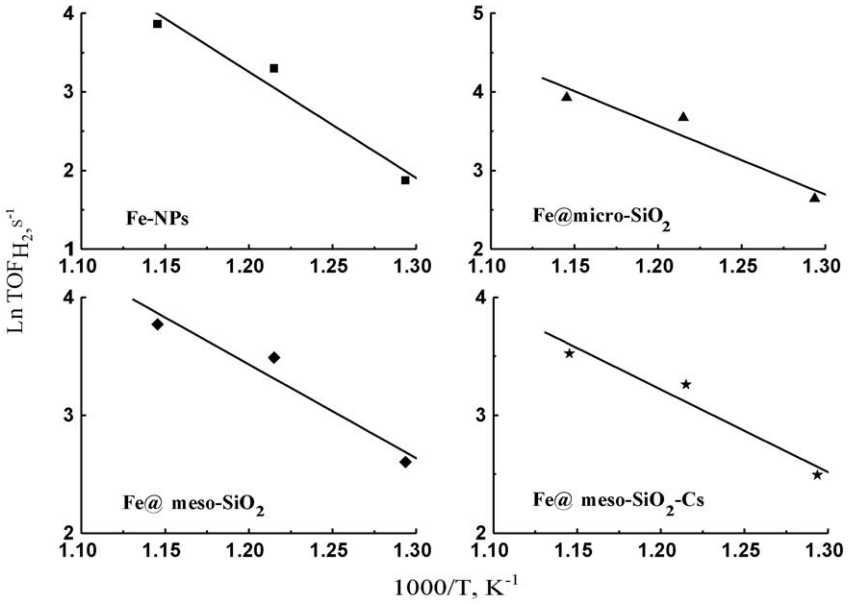

Fig. 11. Arrhenius plots of ammonia decomposition over Fe NPs, Fe@micro-SiO_2, Fe@meso-SiO_2 (0.2) and Fe@meso-SiO_2-Cs (0.2) within the temperature range of 823 ± 50 K.

3.7. Structure–performance relationship

It is generally accepted that on metal surfaces, atoms of lower coordination are usually more reactive. For the Fe catalysts, the active sites associated with N_2 dissociation in ammonia synthesis were thought to be the oligo-atomic metal clusters, i.e., C7-sites (with seven nearest neighbors) [42]. In the present study, the density of active sites can vary with factors such as nature of core–shell interaction, size and shape of core particles, degree of core aggregation, and promoting effect of dopant.

It is apparent that the Fe NPs encapsulated in SiO_2 are more active than the naked Fe NPs as well as the MCM-41-supported Ni NPs [34]. On the basis of per unit mass of Fe, it seems unlikely that the Fe cores have more active sites than the naked or MCM-41-supported Ni NPs. This is because the size of cores is similar to that of the fresh naked Fe NPs or even larger than that of the MCM-41-supported Ni NPs. Nevertheless, the core–shell structures can provide a unique environment around the cores and function as microcapsular-like reactors [43–45] in which the space between the cores and internal shell surfaces is enriched with reactant molecules (Fig. 12). The consequence is enhanced adsorption (as indicated in Table 3) and catalytic interaction on the core surfaces. In other words, despite there is a decline in exposure of surface Fe atoms (per unit mass of catalyst), the core–shell catalysts are catalytically more active than the naked or conventional supported ones due to the microcapsular-like structure. The confinement effect of the reactant is closely related to the microcapsular space. Furthermore, the core–shell catalysts show higher thermal stability than the naked or supported NPs owing to the stable SiO_2 shells that effectively prevent the core NPs from aggregate during reaction. It is clear that the difference in catalytic activity observed over the naked NPs, the supported ones and the core–shell structures are mainly due to the variation in catalyst structures and particularly in local reaction environment. Bear in mind that one should make the comparison with caution among these catalysts because the metal loadings as well as dispersions are different across the catalysts.

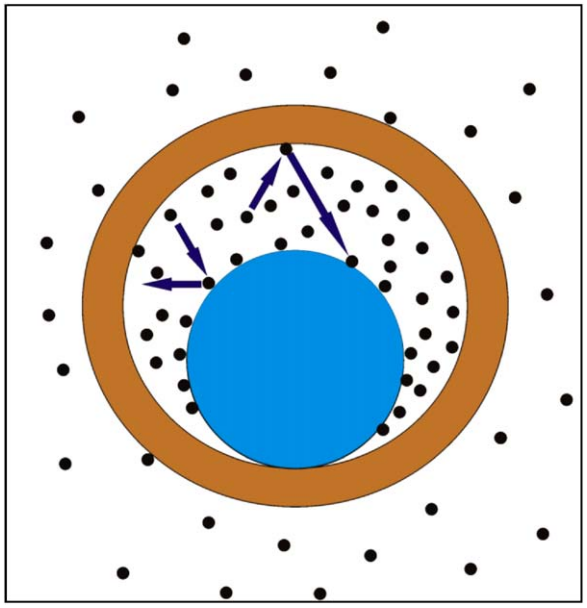

Fig. 12. Schematic of enhanced adsorption and reaction in a microcapsular-like reactor: The round ring of brown color stands for the SiO_2 shell while the small black spheres stand for ammonia molecules and the big blue sphere inside the shell stands for the iron core. (For interpretation of the references to color in this figure legend, the reader is referred to the web version of the article.)

4. Conclusions

We have demonstrated that the Fe NPs enwrapped inside microporous and mesoporous silica are stable catalyst efficient for the production of CO_x-free hydrogen via ammonia decomposition for fuel cell application. With the Fe NPs encapsulated in a porous but stable SiO_2 shell, there is enhanced catalyst performance for the target reaction. We ascribe the effect to the core–shell formation that functions as a microcapsular-like reactor. By tuning the porosity of SiO_2 shells (using C_{18}TMS agent) and/or introducing an appropriate amount of Cs (via pre-deposition or post-impregnation), one can achieve better diffusion efficiency as well as enhanced activity of catalysts. It is noted that aggregation of the core–shell structured nanoparticles is negligible during ammonia decomposition. In other words, the Fe cores are effectively prevented from aggregating into bulk particles at high temperatures of NH_3 decomposition.

Acknowledgement

We acknowledge the financial support of the RGC, HKSAR (RGC 200107).

References

[1] M. Danek, K.F. Jensen, C.B. Murray, M.G. Bawendi, Chem. Mater. 8 (1996) 173–180.
[2] X. Peng, M.C. Schlamp, A.V. Kadavanich, A.P. Alivisatos, J. Am. Chem. Soc. 119 (1997) 7019–7029.
[3] P. Reiss, J. Bleuse, A. Pron, Nano Lett. 2 (2002) 781–784.
[4] V. Skumryev, S. Stoyanov, Y. Zhang, G. Hadjipanayis, D. Givord, J. Nogues, Nature 423 (2003) 850–853.
[5] Y.H. Deng, D.W. Qi, C.H. Deng, X.M. Zhang, D.Y. Zhao, J. Am. Chem. Soc. 130 (2008) 28–29.
[6] F. Teng, Z.J. Tian, G.X. Xiong, Z.S. Xu, Catal. Today 93–95 (2004) 651–657.
[7] K.P. Velikov, A. Moroz, A. van Blaaderen, Appl. Phys. Lett. 80 (2002) 49–51.
[8] J. Luo, M.M. Maye, Y.B. Lou, L. Han, M. Hepel, C.J. Zhong, Catal. Today 77 (2002) 127–138.
[9] F. Grasset, N. Labhsetwar, D. Li, D.C. Park, N. Saito, H. Haneda, O. Cador, T. Roisnel, S. Mornet, E. Duguet, J. Portier, J. Etourneau, Langmuir 18 (2002) 8209–8216.
[10] R.Z. Sorensen, L.J.E. Nielsen, S. Jensen, O. Hansen, T. Johannessen, U. Quaade, C.H. Christensen, Catal. Commun. 6 (2005) 229–232.
[11] D.G. Loffler, L.D. Schmidt, J. Catal. 44 (1976) 244–258.
[12] Y.K. Sun, Y.Q. Yang, C.B. Mullins, W.H. Weinberg, Langmuir 7 (1991) 1689–1694.
[13] M. Grosman, D.G. Loffler, R. Kinet, Catal. Lett. 33 (1987) 87–92.
[14] M.C.J. Bradford, P.E. Fanning, M.A. Vannice, J. Catal. 172 (1997) 479–488.
[15] T.V. Choudhary, C. Sivadinarayana, D.W. Goodman, Catal. Lett. 72 (2001) 197–201.
[16] S.F. Yin, B.Q. Xu, X.P. Zhou, C.T. Au, Appl. Catal. A 277 (2004) 1–9.
[17] W. Arabczyk, J. Zamlynny, Catal. Lett. 60 (1999) 167–171.
[18] J.L. Chen, Z.H. Zhu, Q. Ma, L. Li, V. Rudolph, G.Q. Lu, Catal. Today 148 (2009) 97–102.
[19] R.O. Idem, N.N. Bakhshi, Ind. Eng. Chem. Res. 33 (1994) 2047–2056.
[20] T.V. Choudhary, D.W. Goodman, Catal. Lett. 59 (1999) 93–94.
[21] T.V. Choudhary, D.W. Goodman, J. Catal. 192 (2002) 316–321.
[22] V.R. Choudhary, B.S. Uphade, A.S. Mamman, J. Catal. 172 (1997) 281–293.
[23] J.N. Armor, Appl. Catal. A 176 (1999) 159–176.
[24] R. Metkemeijer, P. Achard, Int. J. Hydrogen Energy 19 (1994) 535–542.
[25] R. Metkemeijer, P. Achard, J. Power Sources 49 (1994) 271–282.
[26] W. Rarog, Z. Kowalczyk, J. Sentek, D. Skladanowski, D. Szmigiel, J. Zielinski, Appl. Catal. A 208 (2001) 213–216.
[27] M.E.E. Abashar, Y.S. Al-Sughair, I.S. Al-Mutaz, Appl. Catal. A 236 (2002) 35–53.
[28] S.F. Yin, B.Q. Xu, S.J. Wang, C.F. Ng, C.T. Au, Catal. Lett. 96 (2004) 113–116.
[29] X. Han, W. Chu, P. Ni, S.Z. Luo, T. Zhang, J. Fuel Chem. Technol. 35 (2007) 691–695.
[30] W. Raróg-Pilecka, D. Szmigiel, Z. Kowalczyk, S. Jodzis, J. Zielinski, J. Catal. 218 (2003) 465–469.
[31] S.F. Yin, B.Q. Xu, W.X. Zhu, C.F. Ng, X.P. Zhou, C.T. Au, Catal. Today 93 (2004) 27–38.
[32] Z. Kowalczyk, J. Sentek, S. Jodzis, M. Muhler, O. Hinrichsen, J. Catal. 169 (1997) 407–414.
[33] A. Jedynak, Z. Kowalczyk, D. Szmigiel, W. Raróg, J. Zieliïnski, Appl. Catal. A: Gen. 237 (2002) 223–226.
[34] Y.X. Li, S.Q. liu, L.H. Yao, W.J. Ji, C.-T. Au, Catal. Commun. 11 (2010) 368–372.
[35] W. Stöber, A. Fink, E. Bohn, J. Colloid Interface Sci. 26 (1968) 62–69.
[36] O. Hinrichsen, Catal. Today 53 (1999) 177–188.
[37] S. Murata, K.I. Aika, J. Catal. 136 (1992) 110–117.
[38] L. Forni, D. Molinari, I. Rossetti, N. Pernicone, Appl. Catal. A 185 (1999) 269–275.
[39] X.K. Li, W.J. Ji, J. Zhao, S.J. Wang, C.T. Au, J. Catal. 236 (2005) 181–189.
[40] H. Cui, G. Hong, X. Wu, Y. Hong, Mater. Res. Bull. 37 (2002) 2155–2163.
[41] J. Cheng, X.M. Ni, H.G. Zheng, B.B. Li, X.J. Zhang, D.E. Zhang, Mater. Res. Bull. 41 (2006) 1424–1429.
[42] J.A. Dumesic, H. Topsoe, M. Boudart, J. Catal. 37 (1975) 513–522.
[43] J. Wu, F.P. Hu, X.D. Hu, Z.D. Wei, P.K. Shen, Electrochim. Acta 53 (2008) 8341–8345.
[44] W.M. Zhang, J.S. Hu, Y.G. Guo, S.F. Zheng, L.S. Zhong, W.G. Song, L.J. Wan, Adv. Mater. 20 (2008) 1160–1165.
[45] S.H. Joo, P.J. Young, C.K. Tsung, Y. Yamada, P.D. Yang, G.A. Somorjai, Nat. Mater. 8 (2009) 126–131.